Energy Storage Materials 89 (2026) 105200

Contents lists available at ScienceDirect

Energy Storage Materials

journal homepage: www.elsevier.com/locate/ensm

Unlocking the kinetic potential of ultra-thick electrodes via mechanism-guided phase-inversion optimization

Chengyu Wang [a,b], Igor Mele [c], Rekha Narayan [a], Miran Gaberščček [a,b], Qiao Hu [d], Tomaž Katrašnik [c], Jože Moškon [a], Aiping Wang [a,*], Robert Dominko [a,b,*]

[a] National Institute of Chemistry, Hajdrihova 19, SI-1000, Ljubljana, Slovenia
[b] Faculty of Chemistry and Chemical Technology, University of Ljubljana, Večna pot 113, SI-1000, Ljubljana, Slovenia
[c] Faculty of Mechanical Engineering, University of Ljubljana, SI-1000 Ljubljana, Slovenia
[d] College of Chemical Engineering, Jiangsu Co-Innovation Center of Efficient Processing and Utilization of Forest Resources, Nanjing Forestry University, Nanjing, Jiangsu 210037, China

ARTICLE INFO

Keywords:
Phase inversion
Thick electrodes
Numerical simulation
Transmission line model (TLM)
Kinetic-dynamic limitation
High-energy-density batteries

ABSTRACT

Bridging the gap between practical and theoretical energy density requires thick electrodes with high areal mass loading, yet these are inherently limited by sluggish kinetics. Phase-inversion method offers a scalable route to low-tortuosity architectures; however, its optimization has been hindered by limited understanding of how solid additives affect the fundamental NMP-H_2O exchange that governs pore formation. Here, using $LiFePO_4$ (LFP) as a model system, we show that regulating solid additives (carbon) enables proper phase separationg dynamics and thus optimized electrode-level performance. Contrary to the convention that thick electrodes require high carbon content, the designed phase-inversion electrodes (PIEs) follow a distinct moderate-carbon optimization strategy. A critical threshold at 6 wt% carbon yields a hybrid microstructure that preserves ion-transport channels while establishing electronic percolation. Specifically, at this moderate content, binder is not excessively consumed by the carbon surface, allowing phase-inversion to proceed effectively to form macro-channels, yet enough carbon is present to bridge the active particles within the polymer matrix. This design avoids structural collapse caused by excessive carbon (disordered pores) and the kinetic isolation of low-carbon formulations (insufficient conductivity). The optimized PIEs (22 mg cm^{-2}) deliver 75% of electrode-level capacity at 1 C and enable an ultra-thick electrode (1.1 mm, 100 mg cm^{-2}) with an exceptional areal capacity of 16 mAh cm^{-2}. These findings establish a mechanism-informed design principle for practical thick electrode manufacturing and provide a scalable strategy extendable to other electrode chemistries.

1. Introduction

Developing high-performance lithium-ion batteries (LIBs) with high energy density and fast-charging capability is essential to meet the growing demands of consumer electronics and electric vehicles [1,2]. A direct approach to achieve higher energy density is to increase the areal loading of electrodes by fabricating thick electrodes, which enhances specific energy and reduces overall production costs. Estimates show that, increasing electrode thickness from 20 to 75 μm results in approximately a 40 wt% improvement in cell-level gravimetric energy density[3,4]. However, increasing electrode thickness inevitably lengthens transport pathways, deteriorating ionic and electronic transport kinetics and dynamics. This hinders the achievement of high energy density and causes a decline in specific capacity, especially under high-rate conditions[1,5]. To address these intrinsic limitations, designing low-tortuosity electrodes with aligned pore structures has been proposed as a promising strategy to facilitate ion and electron transport in thick electrodes[6,7].

Various innovative strategies have been developed to construct low-tortuosity thick electrodes, including hierarchical self-assembling slurry [8,9], templating approaches (e.g., instant microneedle, magnetic, and ice templating)[10–15], evaporation-induced assembly[3,16], 3D printing [17–19], and conductive scaffolds[20–25]. Among these, the phase-inversion method stands out as a leading candidate for industrial implementation due to its scalability and cost-effectiveness [26–30]. Compared with other complex fabrication techniques, phase-inversion

* Corresponding authors.
E-mail addresses: Aiping.Wang@ki.si (A. Wang), Robert.Dominko@ki.si (R. Dominko).

https://doi.org/10.1016/j.ensm.2026.105200
Received 10 March 2026; Received in revised form 18 April 2026; Accepted 5 May 2026
Available online 6 May 2026

requires only a straightforward water immersion step, which is compatible with existing coating lines and enables the formation of hierarchical, interconnected porous networks while facilitating NMP solvent recovery [31,32]. Despite these manufacturing advantages, a critical challenge remains: state-of-the-art phase-inversion electrodes (PIEs) typically rely on high fractions of inactive components (up to 35 wt%) to maintain structural integrity and conductivity [27,33]. This reliance primarily stems from an incomplete understanding of the phase-inversion mechanism in complex composite slurries. Fundamentally, the process is driven by the thermodynamic instability of a ternary system (polymer/solvent/non-solvent). Upon immersion, the rapid exchange between solvent (e.g., NMP) and non-solvent (e.g., H_2O) forces the homogeneous solution into a two-phase region, separating into a polymer-rich phase that solidifies into the matrix and a polymer-lean phase that forms the pores [34–36]. However, the presence of solid particles drastically alters these thermodynamic and kinetic pathways. Without a precise understanding of how conductive agents influence this delicate NMP-H_2O exchange, previous designs have resorted to excessive inactive materials to guarantee performance [27,28,33], severely penalizing electrode-level capacity and overall energy density. Consequently, realizing the full potential of thick PIEs requires a rational formulation design grounded in the fundamental mechanism of phase separation.

While high carbon content is conventionally considered necessary to overcome transport limitations in thick electrodes, we hypothesize that in PIEs, it may be counterproductive, as it disrupts the delicate phase-inversion mechanism and channel formation. Conversely, excessively low carbon content (e.g., < 3 wt%) might yield a "perfect" phase-inversion structure with ideal channels, but fail to provide sufficient electronic percolation. Thus, a unique optimization strategy is required to balance electronic conductivity with the structural integrity of the ionic transport network, avoiding both electronic isolation at low carbon loads and structural collapse at high carbon loads. We propose that a moderate phase-inversion quality, characterized by a hybrid microstructure comprising vertically aligned channels together with an increased fraction of amorphous regions or micropores, provides the optimal compromise. This architecture preserves macroscopic transport pathways while enhancing local electrolyte accessibility and electronic

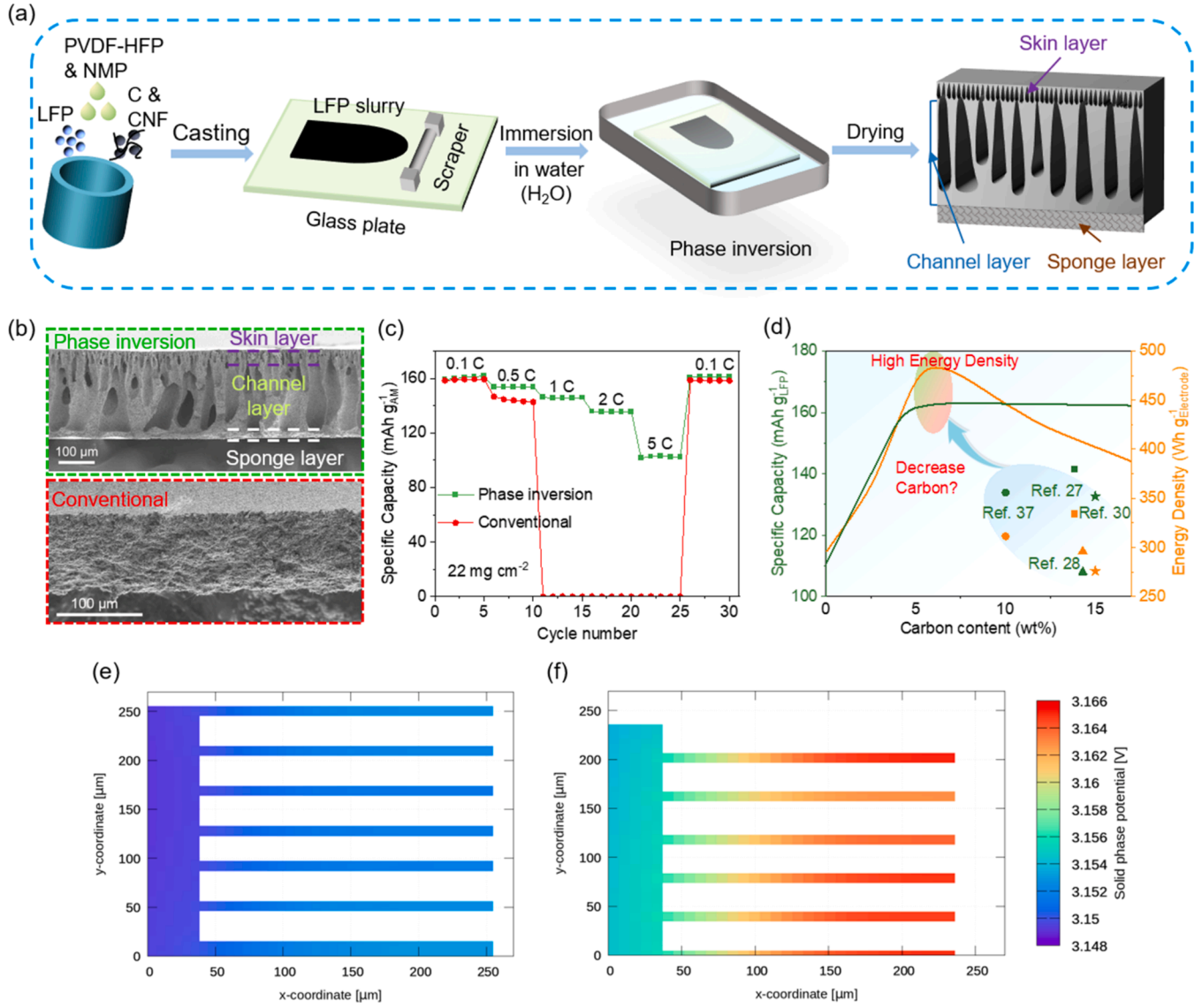

Fig. 1. Phase-inversion-enabled electrode architecture, electrochemical performance, and simulation-assisted insights. (a) Schematic illustration of the phase-inversion process. (b) Cross-sectional SEM images of ConE and PIE. (c) Rate performance at discharge rates from 0.1 to 5 C with a fixed charging rate of 1 C. (d) Trade-off between material-level capacity and electrode-level capacity for PIEs. (e, f) Spatially resolved electrode potential profiles in (e) PIEC-6 and (f) PIEC-3 during discharge at a 2 C rate and DoD = 0.5, with a constant mass loading of 20 mg cm^{-2} but varying thickness.

connectivity.

Here, using $LiFePO_4$ (LFP) as a model system, we unlock the practical potential of PIEs by systematically optimizing their transport kinetics to maximize electrode-level energy density. Our approach clarifies the fundamental interplay between solid additives and the phase-separation thermodynamics that govern pore evolution. By integrating numerical simulations with experimental validation, we demonstrate that efficient transport dynamics can be maintained even at significantly reduced carbon contents. We employ an analytical framework that combines transmission-line modeling (TLM) with a blocking electrolyte in impedance spectroscopy to decouple and quantify the intertwined electronic and ionic transport processes. This analysis identifies a critical threshold at 6 wt% carbon, where simultaneous electronic and ionic percolation is achieved, providing an optimal trade-off between active material utilization and capacity performance. These insights offer a robust design guideline for developing ultra-thick electrodes that deliver both high energy density and fast-charging capabilities, paving the way for broader industrial adoption of phase-inversion manufacturing.

2. Results and discussion

2.1. Phase-inversion demonstration and simulation guidance

To validate the phase-inversion strategy and guide rational electrode formulation design, we combined experimental fabrication with predictive numerical modeling. Fig. 1a illustrates the specific fabrication steps: LFP powder with the morphology shown in Fig. S1 and conductive materials (carbon powder and carbon nanofiber) were mixed in an NMP solution of PVDF-HFP and cast onto a glass plate. Subsequent immersion in a water bath triggered the phase-separation mechanism described above, resulting in the formation of a dense skin layer followed by the growth of vertically aligned channels as NMP diffused out, ultimately leaving a thin sponge layer at the bottom. The resulting PIEs (approximately 275 μm thick) exhibited a 3D hierarchical structure comprising a dense skin, vertical channels, and a sponge layer, which collectively facilitate rapid ionic transport across the electrode (Fig. 1b). Magnified SEM images (Fig. S2) and elemental mapping (Fig. S3) confirmed uniform distribution of LFP and conductive additives. In contrast, conventional electrodes (ConEs, approximately 120 μm) possessed a dense structure that hindered ion transport. Consequently, while both electrodes showed similar capacity at 0.1 C (approximately 160 mAh g^{-1}), ConEs failed at 1 C, whereas PIEs maintained 142 mAh g^{-1} (Fig. 1c). Numerical simulations further elucidated this disparity (Fig. S4), revealing a significantly steeper Li^+ concentration gradient in ConEs compared to PIEs at 50% depth of discharge (DoD) under 0.5 C. This confirms that the channels in PIEs facilitate efficient ion transport, whereas the sluggish kinetics in ConEs lead to severe polarization and capacity loss (Fig. S5).

Despite the inherent transport advantages of PIEs, practical application is currently hindered by the excessive use of inactive components (binder and carbon), which reduces the energy density of PIEs at the electrode level (Fig. 1d) [30,37].

To address this limitation, we used numerical simulations to explore the feasibility of reducing these inactive species, focusing specifically on carbon content. The simulations aimed to determine whether the unique architecture of PIEs could maintain high performance with minimal conductive additives. As shown in Fig. 1e-f, the modeling indicated that carbon content influences the final kinetics and dynamics. Specifically, reducing carbon content from 6 wt% to 3 wt% increased internal polarization from 4 mV to 14 mV at a high C-rate (2 C), implying a potential threshold for minimizing internal losses. This observation suggests that efficient ion and electron transport can be achieved with relatively low carbon loading, without sacrificing the kinetic advantages of the phase-inversion architecture. More importantly, this work advances beyond conventional channel engineering by establishing a mechanism-driven understanding of how solid composition-particularly high-surface-area carbon- regulates phase separation, pore architecture, and coupled ionic/electronic transport, thereby defining an optimal carbon-content regime as a universal design principle for high-energy-density phase-inversion electrodes.

2.2. Microstructural modulation and transport kinetics

Guided by simulation insights and previous reports on PIEs, systematic experiments were conducted to investigate the effect of carbon content on the structural evolution and transport properties of PIEs. Electrodes with varying carbon contents (15, 10, 6, and 3 wt%) were prepared at a fixed mass loading of 22 mg cm^{-2}, denoted as PIEC-15/10/6/3.

As shown in the cross-sectional SEM images (Fig. 2a-d), the electrode microstructure undergoes significant evolution governed by the interplay between carbon content and the phase-inversion process. The EDS elemental mapping (Fig. S6) of Fe, C, and O confirms the uniform distribution of all components within the PIEs. At a high carbon content of 15 wt%, the electrode exhibits a 3D-connected network with a less-ordered channel morphology. As carbon content decreases, the channels become progressively more defined and vertically aligned, resulting in a well-ordered architecture at 3 wt%, characteristic of an ideal phase-inversion structure.

This structural transformation arises from the dual role of the PVDF-HFP binder, which serves both as an adhesive for solid particles and as the structural scaffold for the phase-inversion matrix. LFP particles have a relatively low specific surface area (12.3 m^2 g^{-1}), whereas conductive carbon has a much higher surface area (62 m^2 g^{-1}). Therefore, increasing the ratio of carbon additive significantly raises the total surface area that the fixed amount of binder (5 wt%) should bind together. This consumption of PVDF-HFP for interparticle adhesion reduces the free polymer available to form the continuous skin layer and channel walls during the NMP-H_2O exchange (Fig. 2e). The result is a disrupted phase separation process in which the "finger-like" channels are replaced by a more random, sponge-like porosity. This mechanism is further confirmed by increasing the binder content in high-carbon electrodes (PIEC-15), which restores the regular channel structure (Fig. S7).

Quantitative porosity analysis using mercury intrusion porosimetry (MIP) and theoretical calculations (Eq. S1) confirms the structural evolution caused by varying carbon content (Fig. 2f). As carbon content decreases, total porosity decreases monotonically, accompanied by a marked redistribution of pore sizes (Fig. S8). The fraction of pores smaller than 500 nm reaches a minimum at 3 wt% carbon (Fig. 2g), indicating that a greater proportion of PVDF-HFP remains available to participate in the phase inversion process and form continuous polymer-templated channel walls. Conversely, increasing carbon content to $\geq$ 6 wt% significantly increases the sub-500 nm pore fraction, attributed to intrinsic voids within high surface area carbon aggregates and interparticle packing, reflecting increased binder consumption by conductive additives. Since macro-channels (> 500 nm) and pores smaller than 500 nm arise from fundamentally different formation mechanisms, this systematic shift in pore populations provides quantitative evidence for surface area-driven binder depletion and its role in disrupting the phase inversion process.

In addition, electrolyte wettability measurements further confirm the excellent wetting behavior of PIEs with varying carbon contents (Fig. S9). For example, with PIEC-6, the electrolyte droplet quickly spreads across the electrode surface and almost completely infiltrates the electrode within 2 s, indicating superior electrolyte accessibility.

To determine ion transport kinetics after microstructural modulation, DC polarization measurements (Fig. 3a) were used to quantify the effective ionic diffusivity (D_{eff}) and intrinsic diffusivity (D_0) using Eq. S2-S3 (Fig. S10). This allows quantitative determination of the tortuosity (τ) of the PIEs architectures according to Eq. (1): [38–40]

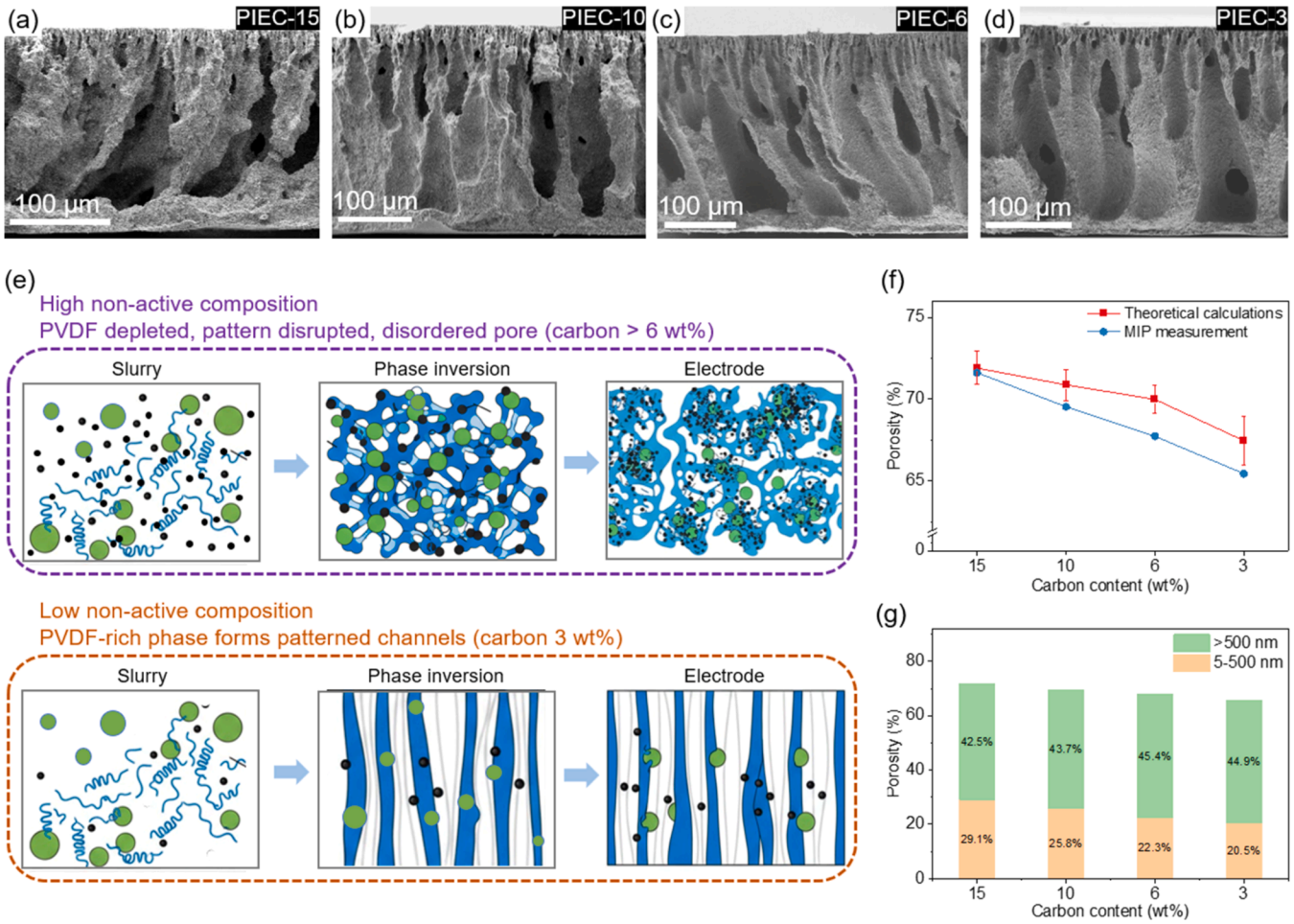

Fig. 2. Carbon-dependent evolution of microstructure and pore characteristics in PIEs. Cross-sectional microstructures of PIEs with varying carbon contents: (a) 15 wt%, (b) 10 wt%, (c) 6 wt%, (d) 3 wt%. (e) Schematic illustration of the evolving role of PVDF-HFP as carbon content decreases. (f) Porosity of PIEs determined by MIP and theoretical calculation. (g) Pore size distribution of PIEs from MIP analysis.

$$\tau = \varepsilon \frac{D_0}{D_{eff}} \tag{1}$$

where ε is the porosity obtained from mercury intrusion porosimetry (MIP). This formulation explicitly links microstructural parameters to ion transport. Lower porosity increases τ, which reduces D_{eff} by elongating and constraining Li^+ pathways. As shown in Fig. 3b-c, D_{eff} remains nearly constant at higher carbon contents. However, when carbon loading is reduced to 3 wt%, a clear decrease of D_{eff} is observed from 3.2 × 10^{-7} cm^2 s^{-1} for PIEC-6 to 1.6 × 10^{-7} cm^2 s^{-1} for PIEC-3. Correspondingly, tortuosity (Fig. 3d) increases substantially from 2.4 (PIEC-6) to 4.7 (PIEC-3). This indicates that while PIEC-3 exhibits highly ordered channels, its lower porosity limits overall transport. In contrast, introducing a moderate amount of carbon (6 wt%) disrupts the perfectly aligned channels to a controlled extent, forming a highly interconnected hybrid pore network that combines the advantages of vertical alignment with enhanced accessibility of a sponge-like structure, thereby promoting efficient ionic diffusion.

To further investigate Li^+ diffusion dynamics within these evolving microstructures, cyclic voltammetry (CV) measurements were conducted. As shown in the CV curves (Fig. S11), the current (i) and scan rates (v) follow the law[41]:

$$i = av^b \tag{2}$$

where a and b are adjustable parameters. Specifically, a b-value of 0.5 indicates a diffusion-controlled process, while a b-value of 1.0 corresponds to a surface-controlled process [42]. From the log(i) versus log(v) profiles (Fig. 3e), the b-values of both cathodic and anodic peaks are approximately 0.56, confirming diffusion-controlled kinetics.

The Li^+ diffusion coefficients (D_{Li^+}) derived from CV (Fig. 3f, Eq. S4, Fig. S12) further indicate that PIEC-6 achieves a superior D_{Li^+} compared to PIEC-3, with negligible improvement at higher carbon loadings. This reinforces the conclusion that a 6 wt% carbon content represents a critical threshold for optimizing electrode-level performance of PIEs. It creates an optimal microstructural balance, providing sufficient disorder to enhance electrolyte permeability without requiring excessive inactive mass that characterizes reported PIEs. Notably, these results indicate that a perfectly aligned channel architecture alone does not guarantee optimal electrochemical performance. Although the vertically aligned macro-channels in PIEC-3 facilitate through-plane ion transport, the reduced fraction of sub-500 nm pores significantly hinders uniform electrolyte distribution across the surfaces of LFP particles. Consequently, ion transport becomes locally diffusion-limited despite the presence of continuous channels. This explains why PIEC-3, despite its well-defined phase-inversion structure, exhibits inferior transport kinetics compared to PIEC-6.

2.3. Decoupling electronic and ionic transport dynamics

In the previous section, we established the macroscopic influence of microstructure on transport kinetics in PIEs. However, the electrochemical response remains inherently complex, involving coupled processes such as ionic transport, electronic conduction, and charge-

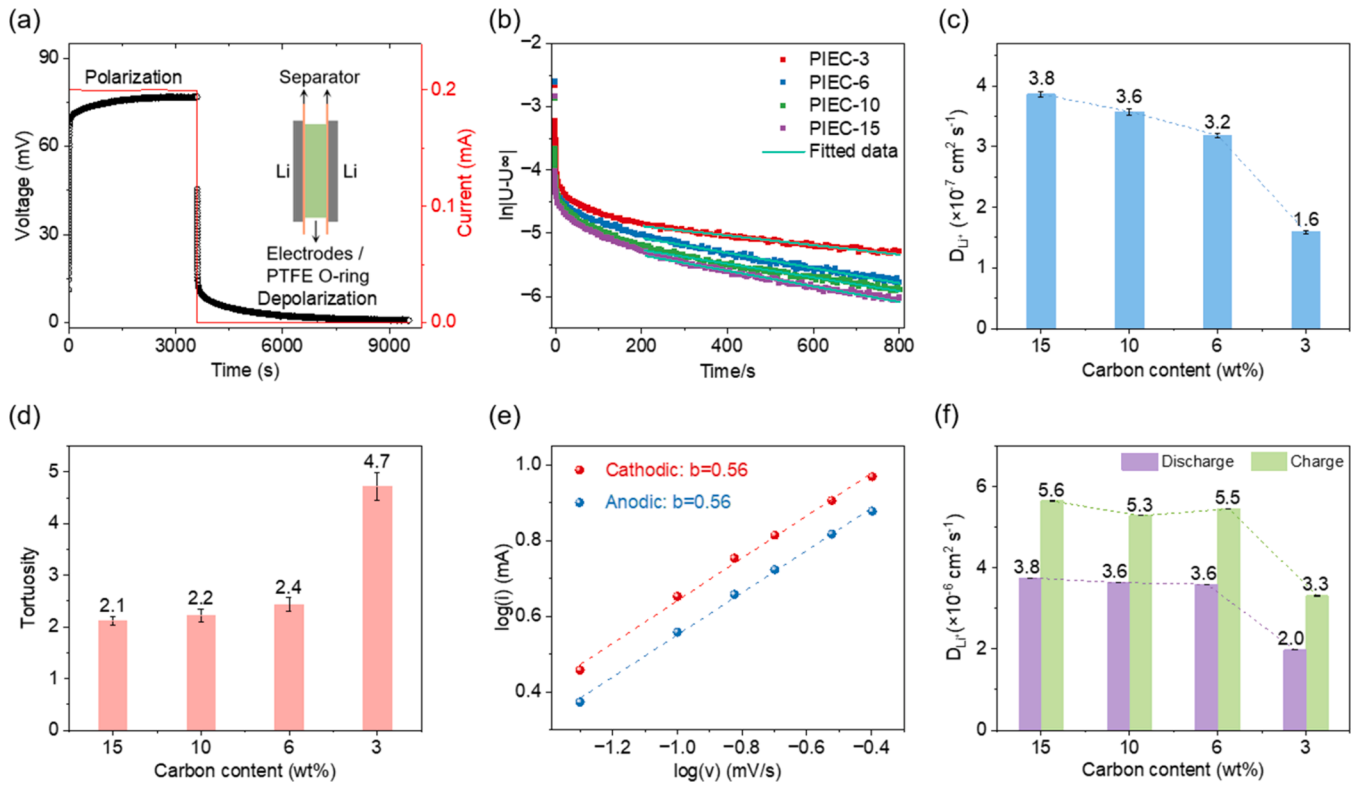

Fig. 3. Carbon-dependent ionic transport behavior in PIEs. (a) Schematic illustration of the DC polarization process in a symmetric cell. (b) Depolarization curves of PIEs with different carbon contents. (c) Comparison of D_{Li^+} calculated from DC polarization data. (d) Calculated tortuosity of PIEs. (e) Determination of the b-value from the relationship between peak current and scan rate based on CV curves. (f) Comparison of D_{Li^+} calculated from CV data.

transfer reactions. To clarify the individual contributions of ionic and electronic transport, these processes were decoupled using electrochemical impedance spectroscopy (EIS) combined with transmission line model (TLM) analysis.

A significant challenge arises in LFP electrodes: phase transformation during electrochemical reactions complicates the separation of charge transfer resistance from impedances. To address this, we used symmetric cells with a blocking electrolyte (10mM $TBAClO_4$ in EC: DMC = 1:1, w/w). This experimental design suppresses faradaic currents, effectively eliminating the charge transfer contribution and allowing us to focus exclusively on transport phenomena.

As shown in Fig. 4a, the TLM used to simulate electrochemical impedance behavior in symmetric cells incorporates contact resistance (Z_{Cont}), internal electron conductive network resistance (R_e), transport resistances of both cations (R_c) and anions (R_a), and chemical capacitance (C_{chem}).

The simulations closely match the experimental impedance response, as shown in Fig. 4b. The high-frequency ($> 10^5$ Hz) intercept on the x-axis represents a pure resistor while the response at the lowest frequencies (< 1 Hz) tends toward a steep (ideally vertical) line, indicating the blocking nature of the electrolyte/pore wall behavior. The deviation from the expected vertical line is attributed to adsorption of species from the electrolyte onto the conductive surface, which is not the focus of this work. It is crucial that this low-frequency region is clearly separated from the 45-degree slope observed in the frequency range of about 1–10^2 Hz, which represents resistance caused by ion migration inside the porous electrode [43,44]. At even higher frequencies (~10^3 Hz), a small arc-like feature appears, which can be attributed to electronic contact at the current collector/composite electrode interface and/or the intrinsic electronic conductivity of bulk LFP particles [44,45]. Since the blocking electrolyte used in this work ensures that no faradaic current flows during the EIS characterization, this arc-like EIS response cannot be related to a charge transfer process, as is usually observed in LIB electrodes.

Fig. 4c shows the ionic and electronic transport resistances of the PIEs, normalized to a PIE thickness of 100 μm. Compared with PIEC-3, PIEC-6 demonstrates significantly improved ionic and electronic transport kinetics. At carbon contents above 6 wt%, the ionic transport resistance remains essentially constant, while the electronic transport resistance continues to decrease. To further support the electronic transport characteristics, the surface conductivity of the PIEs as a function of conductive additive content was measured using the four-probe method, as shown in Fig. 4d. The electrode surface conductivity decreases from 35.9 S m^{-1} to 2.1 S m^{-1} with decreasing carbon content, reflecting the formation of a less interconnected conductive network within the PVDF-HFP matrix and consequently inferior electronic transport.

2.4. Maximizing electrode-level energy density

Having established the fundamental relationship among carbon content, microstructural evolution, and decoupled transport kinetics, we validateed these findings in half-cell configurations. The ultimate goal is to translate the optimized transport balance at 6 wt% carbon into high electrode areal capacity and rate capability.

Fig. 5a presents a comparison of the electrochemical performance of PIEC-15/10/6/3 with an areal mass loading of 22 mg cm^{-2} (corresponding to a practical areal capacity of 3.5 mAh cm^{-2}). Consistent with our kinetic analysis, at 6 wt% carbon, ionic transport - identified as the rate-determining step in thicker electrodes - stabilizes. As a result, PIEC-6, PIEC-10, and PIEC-15 show similar specific capacities at the active-material (AM) level across different C-rates (Fig. S13). However, the key advantage of PIEC-6 is its reduced inactive mass. By achieving comparable AM-level performance with significantly less carbon, PIEC-6 maximizes electrode-level specific capacity, delivering areal capacities of 3.5, 3.4, 3.2, 3.0, and 2.0 mAh cm^{-2} at 0.1, 0.5, 1, 2, and 5 C (1 C = 3.7

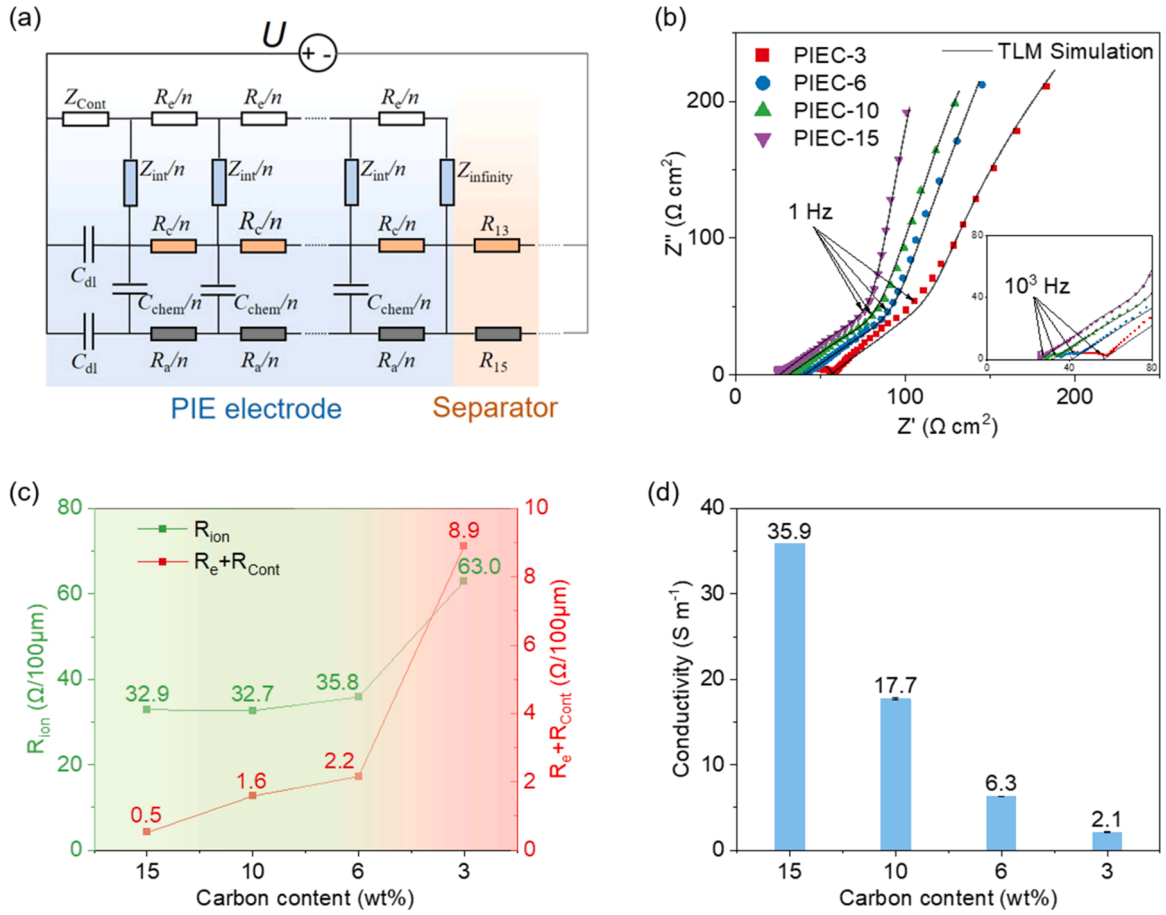

Fig. 4. Decoupling ionic and electronic transport in PIEs using impedance spectroscopy with blocking electrolytes. (a) Transmission line model used to simulate the electrochemical impedance behavior of PIEs. (b) Experimental and simulated Nyquist plots of PIEs' symmetric cells. (c) Ionic and electronic transport resistances of the PIEs, normalized to a reference electrode thickness of 100 μm. (d) Electrical conductivity of the PIEs as a function of conductive agent content.

mA cm^{-2}), respectively, while maintaining near-theoretical Coulombic efficiencies across all rates (Fig. S14a).

This optimized formulation also demonstrates excellent durability. PIEC-6 exhibits cycling stability comparable to higher-carbon counterparts (PIEC-10/15), maintaining a high discharge capacity of 3.0 mAh cm^{-2} with 95% retention after 200 cycles at 1 C (Fig. 5b). The stable charge-discharge profiles at the 1st, 50th, 100th, and 200th cycles (Fig. S15) further confirm the reversibility of the electrochemical reactions within this optimized architecture. Furthermore, post-mortem characterization (Fig. 5c) reveals that the PIEC-6 electrode maintains its structural integrity, with the well-defined channel architecture remaining intact and free from discernible collapse, thereby validating its mechanical robustness and structural stability.

To push the limits of this design, we evaluated the rate performance of PIEC-6 at increasing mass loadings (Fig. 5d). Even at a loading of 35 mg cm^{-2}, the specific capacity remains stable at low rates ($\leq$ 1 C), with only minor decreases at higher current densities ($>$ 2 C), while high Coulombic efficiencies are maintained across all rates (Fig. S14b). Most impressively, we fabricated an ultra-thick PIEC-6 electrode (1.1 mm thickness, 100 mg cm^{-2} loading, approximately 16 mAh cm^{-2} practical areal capacity) that achieved an exceptional areal capacity of 13 mAh cm^{-2} at a high current density of 17 mA cm^{-2} (Fig. 5e). Compared with other reported LFP-based thick electrodes, PIEC-6 demonstrates superior electrode-level rate capability (Fig. 5f), validating our strategy of resolving the carbon-structure trade-off to unlock the full potential of phase-inversion electrodes.

3. Conclusion

In this work, we addressed the critical trade-off between transport kinetics and energy density in PIEs by elucidating the fundamental mechanism governing their microstructural evolution. We demonstrated that, although the phase-inversion process inherently creates superior low-tortuosity channels compared to conventional electrodes, its efficacy is highly sensitive to the solid content in the slurry. Specifically, we found that excessive carbon additives disrupt the delicate NMP-H_2O exchange, degrading the hierarchical channel structure into a disordered network.

Guided by predictive numerical simulations and validated through rigorous microstructural and electrochemical analysis, we established that a moderate phase-inversion quality achieved at a critical carbon content of 6 wt% provides the optimal balance. This formulation creates a hybrid microstructure that retains essential vertical channels for bulk ionic transport while introducing sufficient amorphous microporosity to ensure robust electronic percolation. This insight overturns the conventional approach that maximizing carbon content is necessary for thick electrodes.

Leveraging this mechanism-guided design, we minimized inactive mass without compromising kinetics. The optimized PIEC-6 electrode delivered superior electrode-level capacity (128 mAh g^{-1} at 1 C) and excellent cycling stability (95% retention after 200 cycles). Notably, this strategy enabled the fabrication of an ultra-thick electrode (1.1 mm, 100 mg cm^{-2}) capable of delivering an exceptional areal capacity of 16 mAh cm^{-2}. These findings provide a clear, mechanism-based design principle for the practical upscaling of high-energy-density thick electrodes,

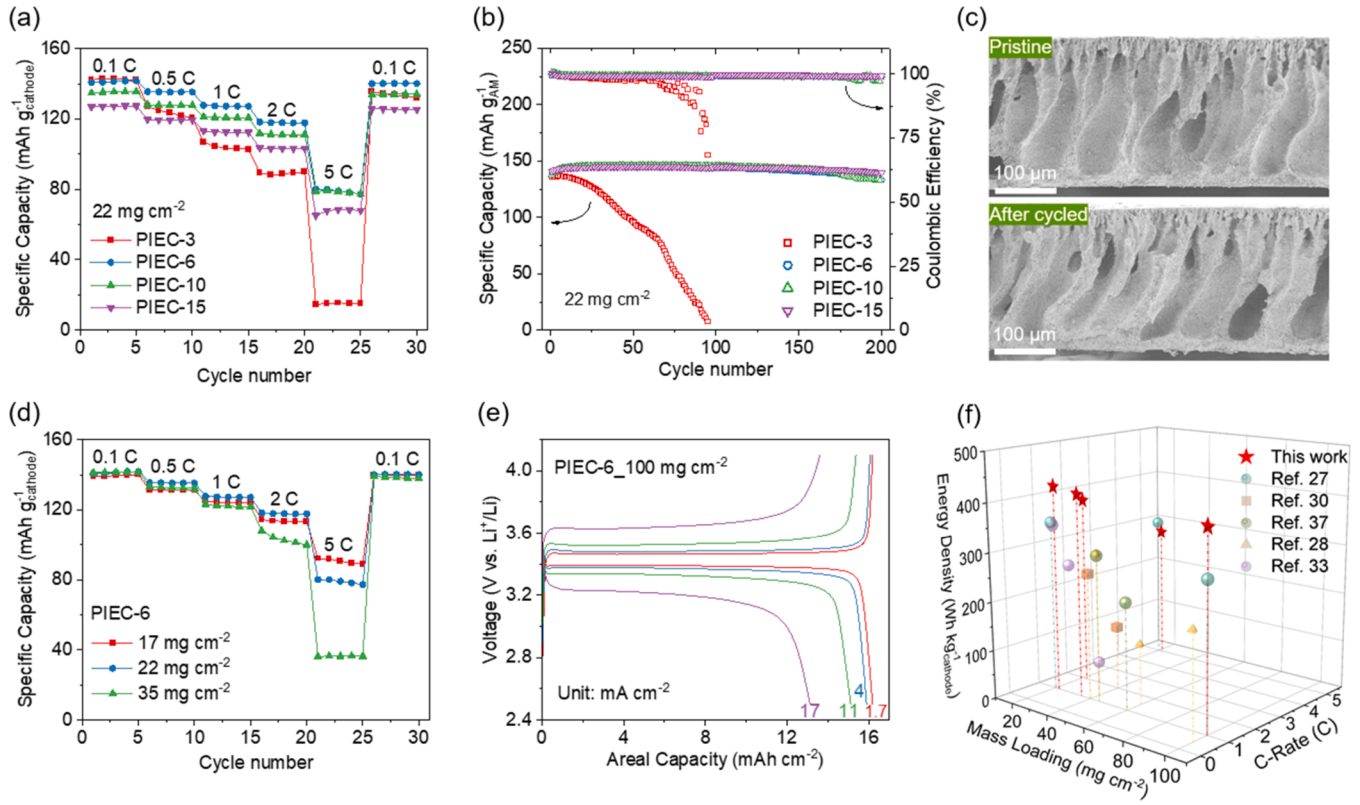

Fig. 5. Electrochemical performance of designed PIEs based on phase-inversion dyanmics regulation. (a) Rate performance of PIEs with various carbon contents. (b) Cycling performance of PIEs at 1 C. (c) Cross-sectional microstructure of PIEC-6 (22 mg cm^{-2}) before and after 200 cycles. (d) Rate performance of PIEC-6 with different areal mass loadings. (e) Charge-discharge profiles of PIEC-6 with a mass loading of 100 mg cm^{-2} (1 C = 17 mA cm^{-2}). (f) Electrochemical performance comparison of our designed PIEC-6 with literature-reported LFP-based thick electrodes.

paving the way for the next generation of high-performance energy storage systems.

4. Experiment section

4.1. Preparation of thick electrodes

A commercial $LiFePO_4$ powder (LFP, P198-S13, Shenzhen Kejing Star Technology Co., Ltd.) was used as received. The LFP powder was blended with carbon black (CB, C—NERGY™ Super C65, IMERYS S.A.) and carbon nanofiber (CNF, PR-25-XT-LHT, Sigma Aldrich), and dispersed in 1-Methyl-2-pyrrolidone (NMP, Sigma Aldrich) containing 5 wt% Poly(vinylidene fluoride-co-hexafluoropropylene) (PVDF-HFP, Solef® 21216, Solvay) and 1 wt% polyvinylpyrrolidone (PVP, K30, Sigma-Aldrich). The detailed compositions are listed in Table S1. The slurry was homogenized by ball milling (PM 200, Retsch® GmbH) for 2 h. For the phase-inversion electrodes (PIEs), a homogeneous slurry was cast onto a glass plate and immediately immersed in water at room temperature (~25 °C) for 1 h to allow phase inversion. The resulting PIEs were collected and dried at 60 °C for 12 h. The mass loading was controlled by adjusting the doctor blade height, with specific values listed in Table S2. For comparison, conventional electrodes were prepared by casting the slurry onto carbon-coated aluminum foil (Armor, France), followed by drying at 60 °C for 12 h.

4.2. Characterization

Morphology and elemental mapping of the samples were examined using a Supra 35 Carl Zeiss FE-SEM (field emission-scanning electron microscope) equipped with an Ultim Max 100 EDX (Energy Dispersive X-ray spectroscopy) detector. The accelerating voltage was set to 2/10 kV for SEM/EDX. The phase purity and crystal structure of LFP were checked using a PANalytical X'Pert PRO X-ray powder diffractometer (Cu Kα1 radiation, $\lambda = 1.5406$ Å). Surface area and pore size distribution were measured with a Mercury Intrusion Porosimeter (MicroActive AutoPore V 9600, Micromeritics Instrument Corporation) in a pressure range of 0.1 to 30,000 psia, with a sample mass of 0.5 to 1 g. The electronic conductivities of the electrode (ø = 10 mm) were measured by the four-point probe method using a semiconductor characterization system (ST2263, Suzhou Lattice Electronics).

4.3. Cell assembly and electrochemical measurements

All cells were assembled in an Ar-filled glovebox ($H_2O/O_2 < 1$ ppm) using LP30 electrolyte (1.0 M $LiPF_6$ in EC:DMC = 1:1, v/v, 60 μL per cell) and a polypropylene membrane (Celgard 3501). Electrochemical tests were carried out using a BioLogic potentiostat (VMP3) at 25 °C. Electrochemical impedance spectroscopy(EIS) was performed in pouch cells over a frequency range of 10^{-1} – 10^6 Hz with an amplitude of 5 mV, using a 10 mM tetrabutylammonium perchlorate ($TBAClO_4$, Sigma Aldrich) solution (10 mM $TBAClO_4$ in EC:DMC = 1:1, w/w) as the electrolyte. Other electrochemical tests, including cyclic voltammetry (CV), galvanostatic charge–discharge, and DC-depolarization tests, were conducted in CR2032 coin cells.

CRediT authorship contribution statement

Chengyu Wang: Writing – original draft, Visualization, Methodology, Investigation, Formal analysis, Data curation, Conceptualization. **Igor Mele:** Methodology, Formal analysis. **Rekha Narayan:** Methodology, Investigation, Formal analysis. **Miran Gaberšček:** Methodology, Formal analysis, Data curation. **Qiao Hu:** Methodology, Formal

analysis. **Tomaž Katrašnik:** Methodology, Formal analysis. **Jože Moškon:** Methodology, Formal analysis. **Aiping Wang:** Writing – review & editing, Supervision, Methodology, Conceptualization. **Robert Dominko:** Writing – review & editing, Supervision, Project administration, Methodology, Funding acquisition.

Declaration of competing interest

The authors declare that they have no known competing financial interests or personal relationships that could have appeared to influence the work reported in this paper.

Acknowledgement

The authors acknowledge the financial support from the Slovenian Research and Innovation Agency through grant P2-0423. AW acknowledge the financial support from the Marie Skłodowska-Curie Actions Postdoctoral Fellowships under Grant Agreement No 101204508. The authors acknowledge partial support from the Republic of Slovenia, Ministry of Higher Education, Science and Innovation, and from the European Union – NextGenerationEU in the framework of the project HyBReED, that is part of the Slovenian Recovery and Resilience Plan. The authors are grateful to Nemanja Lataš for XPS measurements.

Supplementary materials

Supplementary material associated with this article can be found, in the online version, at doi:10.1016/j.ensm.2026.105200.

Data availability

Data will be made available on request.

References

[1] C.D. Quilty, D. Wu, W. Li, et al., Electron and ion transport in lithium and lithium-ion battery negative and positive composite electrodes, Chem. Rev. 123 (2023) 1327–1363, https://doi.org/10.1021/acs.chemrev.2c00214.
[2] M. Winter, B. Barnett, K. Xu, Before Li ion batteries, Chem. Rev. 118 (2018) 11433–11456, https://doi.org/10.1021/acs.chemrev.8b00422.
[3] Y. Kuang, C. Chen, D. Kirsch, et al., Thick electrode batteries: principles, opportunities, and challenges, Adv. Energy Mater. 9 (2019) 1901457, https://doi.org/10.1002/aenm.201901457.
[4] J. Wu, X. Zhang, Z. Ju, et al., From fundamental understanding to engineering design of high-performance thick electrodes for scalable energy-storage systems, Adv. Mater. 33 (2021) 2101275, https://doi.org/10.1002/adma.202101275.
[5] Z. Ju, T. Zheng, J. Calderon, et al., Scalable fast-charging aligned battery electrodes enabled by bidirectional freeze-casting, Nano Lett. 23 (2023) 8787–8793, https://doi.org/10.1021/acs.nanolett.3c03040.
[6] X. Liu, Y. Zeng, W. Yuan, et al., Advances in multi-scale design and fabrication processes for thick electrodes in lithium-ion batteries, Energy Rev. 3 (2024) 100066, https://doi.org/10.1016/j.enrev.2023.100066.
[7] D.J. Arnot, K.S. Mayilvahanan, Z. Hui, et al., Thick electrode design for facile electron and ion transport: architectures, advanced characterization, and modeling, Acc. Mater. Res. 3 (2022) 472–483, https://doi.org/10.1021/accountsmr.1c00281.
[8] Z. Zhang, J. Mo, P. Yu, et al., High-performance flexible sulfur cathodes with robust electrode skeletons built by a hierarchical self-assembling slurry, Adv. Sci. 9 (2022) 2201881, https://doi.org/10.1002/advs.202201881.
[9] X. Fu, Y. Zhou, J. Huang, et al., Rethinking the electrode multiscale microstructures: a review on structuring strategies toward battery manufacturing genome, Adv. Energy Mater. 13 (2023) 2301385, https://doi.org/10.1002/aenm.202301385.
[10] J. Billaud, F. Bouville, T. Magrini, et al., Magnetically aligned graphite electrodes for high-rate performance Li-ion batteries, Nat. Energy 1 (2016) 16097, https://doi.org/10.1038/nenergy.2016.97.
[11] J.S. Sander, R.M. Erb, L. Li, et al., High-performance battery electrodes via magnetic templating, Nat. Energy 1 (2016) 16099, https://doi.org/10.1038/nenergy.2016.99.
[12] Z. Ju, Y. Zhu, X. Zhang, et al., Understanding thickness-dependent transport kinetics in nanosheet-based battery electrodes, Chem. Mater. 32 (2020) 1684–1692, https://doi.org/10.1021/acs.chemmater.9b05396.
[13] Z. Han, S. Li, R. Xiong, et al., Low tortuosity and reinforced concrete type ultra-thick electrode for practical lithium–Sulfur batteries, Adv. Funct. Mater. 32 (2022) 2108669, https://doi.org/10.1002/adfm.202108669.
[14] T. Ma, Z. Wang, D. Wu, et al., High-areal-capacity and long-cycle-life all-solid-state battery enabled by freeze drying technology, Energy Environ. Sci. 16 (2023) 2142–2152, https://doi.org/10.1039/D3EE00420A.
[15] W. Cai, Z. Zhu, C. Ma, et al., Acupuncture-inspired active-material microenvironment engineering for high-throughput thick electrodes by instant microneedle templating, Adv. Mater. 38 (2026) e15343, https://doi.org/10.1002/adma.202515343.
[16] Y. Zhu, Z. Ju, X. Zhang, et al., Evaporation-induced vertical alignment enabling directional ion transport in a 2D-nanosheet-based battery electrode, Adv. Mater. 32 (2020) 1907941, https://doi.org/10.1002/adma.201907941.
[17] D. Cao, Y. Xing, K. Tantratian, et al., 3D Printed high-performance lithium metal microbatteries enabled by nanocellulose, Adv. Mater. 31 (2019) 1807313, https://doi.org/10.1002/adma.201807313.
[18] W.J. Scheideler, J. Im, Recent advances in 3D printed electrodes – Bridging the nano to mesoscale, Adv. Sci. 12 (2025) 2411951, https://doi.org/10.1002/advs.202411951.
[19] Y. Fu, A. Zhang, J. Ma, et al., Ultrathick $LiCoO_2$ cathodes with low tortuosity and accelerated kinetics enable high areal capacity and long-life customable batteries, Energy Storage Mater. 78 (2025) 104291, https://doi.org/10.1016/j.ensm.2025.104291.
[20] S.-H. Park, P.J. King, R. Tian, et al., High areal capacity battery electrodes enabled by segregated nanotube networks, Nat. Energy 4 (2019) 560–567, https://doi.org/10.1038/s41560-019-0398-y.
[21] H. Sun, L. Mei, J. Liang, et al., Three-dimensional holey-graphene/niobia composite architectures for ultrahigh-rate energy storage, Science 356 (2017) 599–604, https://doi.org/10.1126/science.aam5852.
[22] C. Chen, Y. Zhang, Y. Li, et al., Highly conductive, lightweight, low-tortuosity carbon frameworks as ultrathick 3D current collectors, Adv. Energy Mater. 7 (2017) 1700595, https://doi.org/10.1002/aenm.201700595.
[23] J. Xu, J. Lei, N. Ming, et al., Rational design of wood-structured thick electrode for electrochemical energy storage, Adv. Funct. Mater. 32 (2022) 2204426, https://doi.org/10.1002/adfm.202204426.
[24] B. Shi, Y. Shang, Y. Pei, et al., Low tortuous, highly conductive, and high-areal-capacity battery electrodes enabled by through-thickness aligned carbon Fiber framework, Nano Lett. 20 (2020) 5504–5512, https://doi.org/10.1021/acs.nanolett.0c02053.
[25] Y. Kuang, C. Chen, G. Pastel, et al., Conductive cellulose nanofiber enabled thick electrode for compact and flexible energy storage devices, Adv. Energy Mater. 8 (2018) 1802398, https://doi.org/10.1002/aenm.201802398.
[26] X. Yang, Y. Chen, M. Wang, et al., Phase inversion: a universal method to create high-performance porous electrodes for nanoparticle-based energy storage devices, Adv. Funct. Mater. 26 (2016) 8427–8434, https://doi.org/10.1002/adfm.201604229.
[27] J. Wang, M. Wang, N. Ren, et al., High-areal-capacity thick cathode with vertically-aligned micro-channels for advanced lithium ion batteries, Energy Storage Mater. 39 (2021) 287–293, https://doi.org/10.1016/j.ensm.2021.04.030.
[28] J. Wu, Z. Ju, X. Zhang, et al., Ultrahigh-capacity and scalable architected battery electrodes via tortuosity modulation, ACS Nano 15 (2021) 19109–19118, https://doi.org/10.1021/acsnano.1c06491.
[29] P. Karanth, M. Weijers, P. Ombrini, et al., A phase inversion strategy for low-tortuosity and ultrahigh-mass-loading nickel-rich layered oxide electrodes, Cell Rep. Phys. Sci. 5 (2024) 101972, https://doi.org/10.1016/j.xcrp.2024.101972.
[30] Y. Zhang, Y. Xiao, L. Chen, et al., A strategy to build high-performance thick electrodes for lithium-ion batteries with enhanced compressive modulus and regulated tortuosity in the phase-inversion process, J. Mater. Chem. A 12 (2024) 16537–16545, https://doi.org/10.1039/D4TA00589A.
[31] P. van de Witte, P.J. Dijkstra, J.W.A. van den Berg, et al., Phase separation processes in polymer solutions in relation to membrane formation, J. Memb. Sci. 117 (1996) 1–31, https://doi.org/10.1016/0376-7388(96)00088-9.
[32] S. Wongchitphimon, R. Wang, R. Jiraratananon, et al., Effect of polyethylene glycol (PEG) as an additive on the fabrication of polyvinylidene fluoride-co-hexafluropropylene (PVDF-HFP) asymmetric microporous hollow fiber membranes, J. Memb. Sci. 369 (2011) 329–338, https://doi.org/10.1016/j.memsci.2010.12.008.
[33] Y. Zhang, M. Shahriar, S. Hu, Acoustic particle patterning aided by phase-inversion for efficient structuring of low-tortuosity battery electrodes, Batter. Supercaps 8 (2025) e202400745, https://doi.org/10.1002/batt.202400745.
[34] C.A. Smolders, A.J. Reuvers, R.M. Boom, et al., Microstructures in phase-inversion membranes. Part 1. Formation of macrovoids, J. Memb. Sci. 73 (1992) 259–275, https://doi.org/10.1016/0376-7388(92)80134-6.
[35] T.-H. Young, L.-W. Chen, Pore formation mechanism of membranes from phase inversion process, Desalination 103 (1995) 233–247, https://doi.org/10.1016/0011-9164(95)00076-3.
[36] in M.K. Purkait, M.K. Sinha, P. Mondal, et al., in, in: M.K. Purkait, M.K. Sinha, P. Mondal, R. Singh (Eds.), Interface Science and Technology, Interface Science and Technology, 25, Elsevier, 2018, pp. 1–37, https://doi.org/10.1016/B978-0-12-813961-5.00001-2.
[37] J. Wu, Z. Ju, X. Zhang, et al., Low-tortuosity thick electrodes with active materials gradient design for enhanced energy storage, ACS Nano 16 (2022) 4805–4812, https://doi.org/10.1021/acsnano.2c00129.
[38] L. Li, R.M. Erb, J. Wang, et al., Fabrication of low-tortuosity ultrahigh-area-capacity battery electrodes through magnetic alignment of emulsion-based slurries, Adv. Energy Mater. 9 (2019) 1802472, https://doi.org/10.1002/aenm.201802472.
[39] F. Pouraghajan, H. Knight, M. Wray, et al., Quantifying tortuosity of porous Li-ion battery electrodes: comparing polarization-interrupt and blocking-electrolyte

methods, J. Electrochem. Soc. 165 (2018) A2644–A2653, https://doi.org/10.1149/2.0611811jes.
[40] K.S. Saqib, J.H. Choi, S. Park, et al., High-mass loading nickel-rich cathode electrode design incorporating multidimensional carbon conductive additives to minimize ohmic contact resistance for high-performance lithium-ion batteries, ACS Appl. Mater. Interfaces 17 (2025) 48429–48439, https://doi.org/10.1021/acsami.5c12663.
[41] H. Lindström, S. Södergren, A. Solbrand, et al., Li^+ ion insertion in TiO_2 (Anatase). 2. Voltammetry on nanoporous films, J. Phys. Chem. B 101 (1997) 7717–7722, https://doi.org/10.1021/jp970490q.
[42] V. Augustyn, J. Come, M.A. Lowe, et al., High-rate electrochemical energy storage through Li+ intercalation pseudocapacitance, Nat. Mater 12 (2013) 518–522, https://doi.org/10.1038/nmat3601.
[43] M. Gaberscek, J. Moskon, B. Erjavec, et al., The importance of interphase contacts in Li ion electrodes: the meaning of the high-frequency impedance arc, Electrochem. Solid-State Lett. 11 (2008) A170, https://doi.org/10.1149/1.2964220.
[44] J. Moškon, M. Gaberšček, Transmission line models for evaluation of impedance response of insertion battery electrodes and cells, J. Power Sources Adv. 7 (2021) 100047, https://doi.org/10.1016/j.powera.2021.100047.
[45] A. Shodiev, M. Chouchane, M. Gaberscek, et al., Deconvoluting the benefits of porosity distribution in layered electrodes on the electrochemical performance of Li-ion batteries, Energy Storage Mater. 47 (2022) 462–471, https://doi.org/10.1016/j.ensm.2022.01.058.